Sustainable and atomically dispersed iron electrocatalysts derived from nitrogen- and phosphorus-modified woody biomass for efficient oxygen reduction

Yahao Li[a#], Daobin Liu[b#], Jie Gan[c], Xuezhi Duan[c,*], Ketao Zang[d], Magnus Rønning[a], Li Song[b], Jun Luo[d], De Chen[a,*]

[a] Department of Chemical Engineering, Norwegian University of Science and Technology, N-7491 Trondheim, Norway.
[b] National Synchrotron Radiation Laboratory, CAS Center for Excellence in Nanoscience, University of Science and Technology of China, Hefei, Anhui 230029, China.
[c] State Key Laboratory of Chemical Engineering, East China University of Science and Technology, 130 Meilong Road, Shanghai 200237, China.
[d] Center for Electron Microscopy and Tianjin Key Lab of Advanced Functional Porous Materials, Institute for New Energy Materials & Low-Carbon Technologies, School of Materials, Tianjin University of Technology, Tianjin 300384, China.
[#] These authors contributed equally to this work.

Development of low-cost, efficient and robust electrocatalysts to replace precious platinum catalysts for oxygen reduction reaction (ORR) is urgent to boost the applications of green energy devices such as fuel cells and metal-air batteries. Herein, we report sustainable and cost-effective ORR electrocatalysts with atomically dispersed iron on nitrogen- and phosphorus-doped carbon, prepared by a simple impregnation-pyrolysis of different renewable woody biomass with or without external iron precursor introduction. The protocol endows the catalysts with simultaneously tuned hierarchical pores and active site structures. Accordingly, the prepared sustainable, atomically dispersed iron on nitrogen- and phosphorus-doped carbocatalysts outperform the state-of the-art platinum-based catalyst in alkaline media in terms of ORR activity, selectivity and stability. It presents a key step toward scalable production of sustainable, high performance, non-precious metal ORR electrocatalysts from biomass to replace Pt-based ones in large-scale applications.

1

1. Introduction

Green electrochemical devices like fuel cells and metal-air batteries play a crucial role in energy conversion and storage systems, and their output energy capacity is predominantly determined by the cathodic oxygen reduction reaction (ORR) owing to its sluggish kinetics. [1] Although precious Pt-based catalysts have shown to be high ORR activity, [2] its high cost, scarcity as well as susceptibility to time-dependent drift, crossover effect and CO poisoning are prohibitive to large-scale commercialization. [3, 4] Hence, there is a need to develop either less expensive alternatives or catalysts with higher activity. Accordingly, great efforts have been devoted to searching for cost-effective ORR catalysts to replace Pt-based catalysts, such as non-precious metal [5] or even metal-free catalysts. [3, 6, 7]

Heteroatoms doped carbon materials are promising metal-free electrocatalysts for green and sustainable ORR that attracted many researchers and nitrogen-doped carbon materials are the most intensely studied ones for their effectiveness and unique active site structures. [8] Moreover, introducing another non-metal element into N-doped carbon matrix is reported to be an efficient method to boost the performances of metal-free electrocatalysts, and even endue the electrocatalysts with the ability to catalyze oxygen evolution reactions (OER). One of the successful examples is reported by Titirici and coworkers that co-doping phosphorus and nitrogen could introduce the bi-functionality for both ORR and OER.[9] When non-precious metal elements instead of non-metal elements were introduced into N-doped carbon system, intentionally or accidentally, [10, 11] the activities of the resultant electrocatalysts are largely enhanced. In this category, the single-atom Fe catalysts with MN4 structure [12, 13] have been extensively studied as electrocatalysts towards ORR with demonstrated activity and stability approaching to those of commercial Pt/C catalyst. In addition, despite significant achievements on these catalysts with the activity close or even better than the state-of-the-art Pt/C catalysts in terms of activities [14, 15], the catalysts are still not yet warranted to be low cost, green and implementation in real energy conversion/storage devices.

The issues are readily manifested by tracking the research status of Fe-N-C ORR catalysts. Metal-, nitrogen- and carbon-containing molecular or polymeric precursor, materials with well-defined structures like MOFs [16] and graphene [14, 17, 18] are often employed in the synthesis of isolated metal catalysts, which remains a challenge to isolate iron atoms in nitrogen doped carbon matrix at a large scale but in a cost effective way. In addition, similar to the production of many heterogeneous catalysts, the process is not sustainable, in terms of either toxic or limited resources, or cumbersome procedures for their manufacture. Increasingly, scientists look for green and sustainable catalysts to make process more sustainable by turning to renewable sources such as animals and biomass for catalytic materials, [19, 20] as they are abundant worldwide, sustainable, environment benign and most importantly low costs. [20] Moreover, to make (precious) metal-free catalysts truly competitive with Pt/C, hierarchically porous structure of catalysts is required in electrode, to make active sites highly accessible at the gas liquid and solid interface in electrode. [21] These limitations represent the key obstacle to unambiguously replacing of Pt electrocatalysts by these non-precious metal or metal-free catalysts. [22]

Herein, we report an unambiguously simple and scalable synthesis of single-atom iron dispersed in N and P co-doped carbon (NPC) matrix as sustainable and cost-effective electrocatalysts for the ORR reaction. Three types of woody biomass, i.e., sawdust, wood flakes and pulping fibers (common raw material in paper industry), are applied as green carbon sources. The resultant catalysts possess high specific surface areas around 2000 m^2 g^{-1}, hierarchically porous structures and co-doping of N and P. Aberration-corrected HAADF-STEM measurements reveal atomically dispersed Fe atoms in the NPC derived from pine sawdust, where a small amount of Fe originated directly from the pine dramatically enhances the ORR activity. Inspired by the natural materials, introduction of external iron precursor into the biomass makes electrocatalysts with extraordinary ORR activity superior to the state-of-the-art commercial Pt catalysts, regardless of biomass sources.

3

2. Results and discussion

The fabrication process of NPC using a simple impregnation-pyrolysis method is schematically shown in **Figure 1**a. The as-treated different woody biomass powders from impregnation in the precursor solution followed by drying were pyrolyzed under a NH_3 flow at 1000 °C to form NPC. Cyclic voltammetry (CV) curves of NPC catalysts in Ar-saturated and O_2-saturated 0.1 mol L^{-1} KOH with scan rate of 10 mV s^{-1} were obtained (**Figure 1**b). All samples exhibit oxygen reduction peaks only in O_2-satureated electrolyte. Compared to the N and P co-doped woody briquette derived porous carbon (NP-WB) and N and P co-doped thermo-mechanical pulping biomass fiber derived porous carbon (NP-TMP), the N and P co-
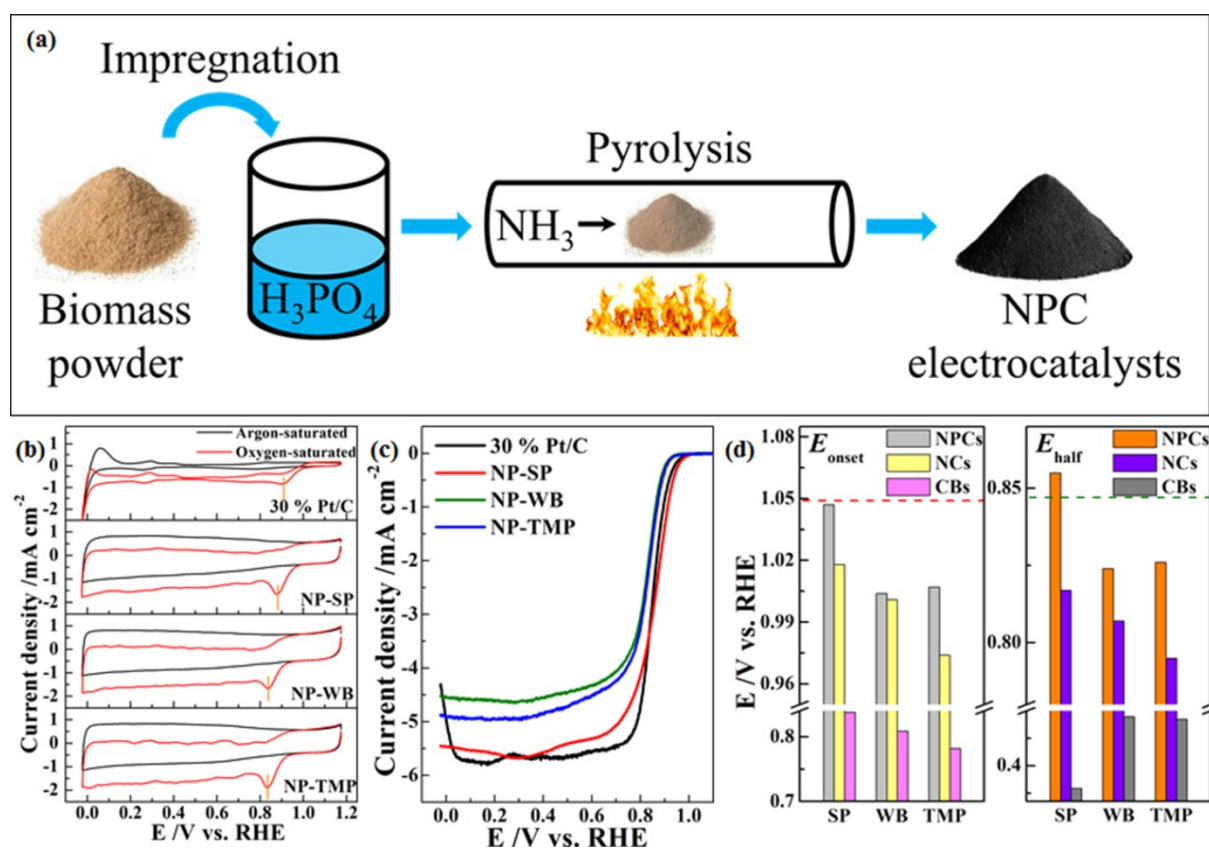

Figure 1. (a) Scheme of NPC production procedure. (b) CV of NPC catalysts and 30 % Pt/C in argon or oxygen saturated 0.1 mol L^{-1} KOH aqueous solution at a scan rate of 10 mV s^{-1}. (c) LSV curves of NPCs in O_2-saturated 0.1 mol L^{-1} KOH at a scan rate of 10 mV s^{-1} with rotating rate of 1600 r.p.m. (d) Bar chart of E_{onset} and E_{half} of NPCs and NCs. The red and green dash line in (d) indicate the E_{onset} and E_{half} of 30 % Pt/C, respectively.

doped sawdust of pine derived porous carbon (NP-SP) exhibits more positive peak at 879 mV, only 21 mV negative than that of commercial 30 % Pt/C catalyst (900 mV), suggesting a high ORR activity of NP-SP.

Linear sweep voltammetry (LSV) tests of NPCs as well as nitrogen doped biomass derived carbons (NCs) and carbonized biomasses (CBs) as reference catalysts were further carried out, and the results are shown in **Figure 1**c and **Figure S1**a and **Figure S1**b in supplementary information. It is obvious that the ORR activities of CBs are very poor that the onset potentials (E_{onset}), half-wave potentials (E_{half}) and limit current density (C_{limit}) are only at around 0.8 V, 0.4 V and 3 mA cm^{-2}, respectively. Similar to the results of many literatures, [23, 24] once N is introduced, the activities are dramatically boosted, where the E_{onset} and E_{half} of NCs are only slightly more negative than those of Pt/C and the C_{limit} is almost doubled those of CBs. When P is further introduced, the ORR activities of NPC catalysts become even better than those of NCs. It can be clearly shown in **Figure 1**d that obvious enhancements are observed when introducing P into the system, where the E_{onset} and E_{half} of NPCs are 20 to 50 mV more positive than those of NCs. This observation is consistent to Guo's reported [9] that P,N co-doping structure will affect the electronic structure of the 'real' active site, the carbon next to N, modify the binding energy of reaction intermediates on it, and thus enhanced the catalytic activity. Surprisingly, the NP-SP exhibited the most positive E_{onset} (1.047 V) and E_{half} (0.855 V) that are even comparable to those of Pt/C (E_{onset} = 1.049 V and E_{half} = 0.847 V) and outperforming many state-of-the-art non-platinum electrocatalysts [6, 11, 24, 25].

To reveal the origin of the outstanding ORR activity of the NP-SP catalyst, different characterizations were carried out. Representative SEM image of NPCs with low magnification in **Figure 2**a shows the initial biomass powder morphology. The size of carbon pellet can be tuned by the initial biomass pellet size. Direct synthesis of carbon pellets will be beneficial for building efficient electrodes by supplying hierarchical structures to reduce the transportation resistance of oxygen and water. High-magnification SEM images in **Figure S2**
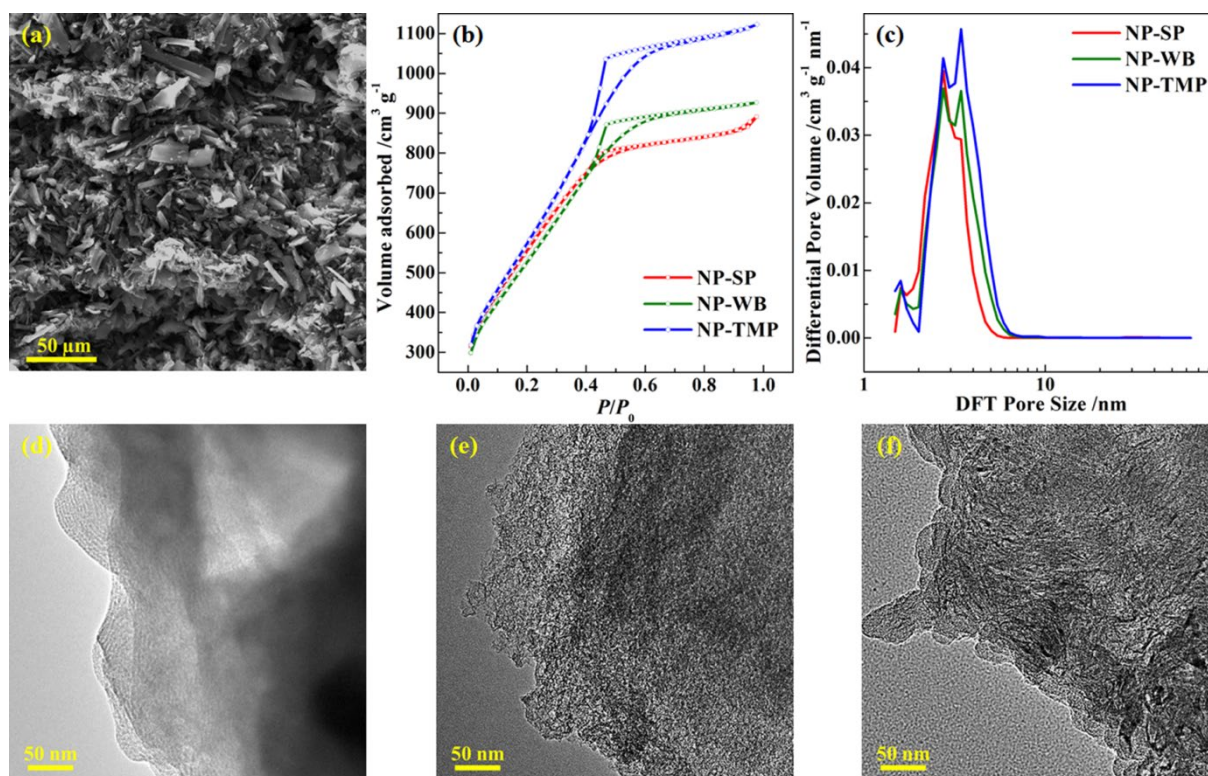
Figure 2. (a)Typical SEM image of NPCs with low magnification. (b) Isotherm and (c) DFT pore size distribution of NPC catalysts. TEM images of NP-SP (d), NP-WB (e) and NP-TMP (f).

Table 1. BET and XPS results of NPC catalysts

Catalysts	SSA $m^2\ g^{-1}$	V_{meso} $cm^3\ g^{-1}$	V_{micro} $cm^3\ g^{-1}$	Elemental (at%)				
				C 1s	O 1s	N 1s	P 2p	Fe 2p
NP-SP	2066	0.95	0.29	91.1	5.8	1.85	0.19	0.04
NP-WB	1970	0.98	0.27	88.3	7.04	3.73	0.65	-
NP-TMP	2164	1.25	0.25	91.9	5.59	1.92	0.22	-

present the NPC catalysts with rough surfaces. TEM images in **Figure 2**d-f and **Figure S3** show that the micro structures of each NPC are different to each others, which may owing to the different wood precursors employed. However, they are all consisting of multiple layers of graphitic sheets, which would be benefit for enhancing the active site accessibility and improving the electron conductivity, respectively. Moreover, N_2 physisorption measurements show that all the catalysts exhibit very high specific surface areas (1970-2164 $m^2\ g^{-1}$, shown in

Table 1). Their isotherms (**Figure 2**b) are of type IV, possessing H2-typed hysteresis loop with characteristic of the channel like mesoporous structure with narrow pore mouth. The corresponding pore size distribution curves (**Figure 2**c) show the three catalysts with typical micro- and meso-porous (i.e., hierarchically porous) structures, whose pore volumes with dominantly contributed by mesopores, being 0.95-1.25 cm^3 g^{-1}, are summarized in **Table 1**. Notably, despite that the superb SSA and hierarchically porous structures in NPCs can endow the catalysts with more accessible active sites and enhance mass transfer at the three-phase interface in the electrodes, the underlying nature of the NP-SP catalysts with much higher ORR activity most likely arises from unique structural and electronic properties of the active sites.

In order to understand this issue, X-ray photoelectron spectroscopy (XPS) and X-ray absorption near edge structure (XANES) measurements were carried out. The XPS surveys in **Figure S1**c clearly display the C 1s and O 1s peaks at around 286 and 530 eV, while peaks for N 1s and P 2p are less obvious. The existences of N and P were confirmed with enlarge curves and the elemental concentration in terms of atom percentage (at%) are summarized in **Figure 3**a and **Table 1**. NP-SP and NP-TMP possess similar amount of N and P contents while about 3.73 at% of N and 0.65 at% of P were found in NP-WB, which are about two to three times higher. The deconvolution of C 1s peaks, N 1s peaks and P 2p peaks were performed and the results are shown in **Figure 3**b, c and e, respectively. C 1s peak can be de-convoluted into four peaks located at around 284.6, 285.4, 286.3 and 288.0 eV, respectively, which can be ascribed to C=C (C1), C-C or C-N or C-P (C2), C-O (C3) and C=O (C4), respectively. [17, 26] C1 is the dominant component in C 1s peaks of all NPCs, while the fractions of C2 and C3 are both quite high, indicating the possible existence of C-N, C-P and C-O bonds. N 1s peak can be de-convoluted into four peaks located at around 398.6, 400.5, 401.3 and 402.0 eV, which correspond to pyridinic N (N1), pyrrolic N (N2), graphitic N (N3) and oxidized pyridinic N
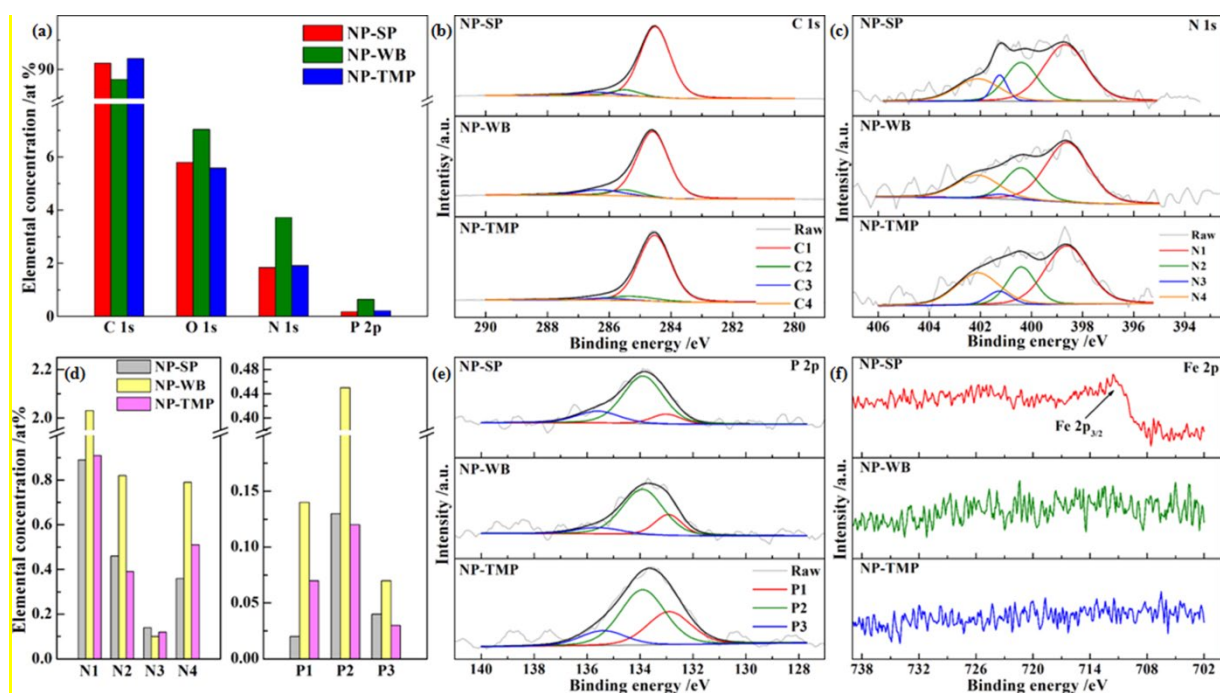
7

Figure 3. (a) Bar chart of elemental concentrations of NPC catalysts. XPS results of NPC catalysts: (b) C 1s peaks, (c) N 1s peaks, (e) P 2p peaks and (f) Fe 2p peaks. (d) Bar chart of deconvolution results of N 1s peaks and P 2p peaks for NPC catalysts.
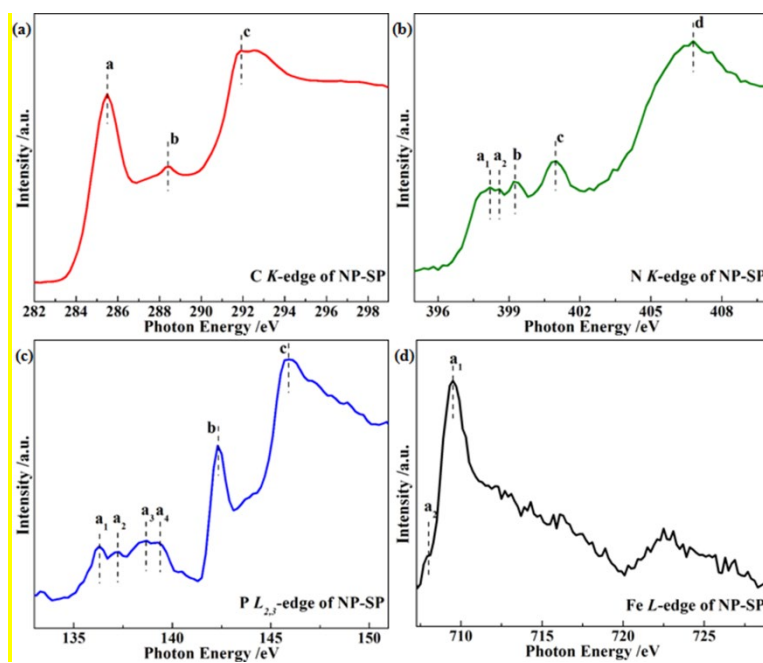

Figure 4. (a) C K-edge, (b) N K-edge, (c) P $L_{2,3}$-edge and (d) Fe L-edge XANES spectra of NP-SP.

Table 2. Deconvolution results of C 1s, N 1s peaks and P 2p peaks of NPC catalysts.

Catalysts	C 1s (at%)				N 1s (at%)				P 2p (at%)		
	C1	C2	C3	C4	N1	N2	N3	N4	P1	P2	P3
NP-SP	79.45	6.26	4.53	0.86	0.89	0.46	0.14	0.36	0.02	0.13	0.04
NP-WB	73.09	6.52	7.97	0.73	2.03	0.82	0.10	0.79	0.14	0.45	0.07
NP-TMP	79.51	8.06	3.03	1.30	0.91	0.39	0.12	0.51	0.07	0.12	0.03

(N4), respectively. [6] These results easily confirms the existence of C-N bonds. It is reported that the pyridinic N and graphitic N are benefit to the ORR activity, [3, 6, 9, 27] while the present of both in all NPCs may lead to their high ORR activities. P 2p peaks can be de-convoluted into three peaks that located at around 132.9 eV (P-C bond, P1), 133.8 eV (P-O bond, P2) and 135.5 eV (metaphosphate, PO_3^-, P3). [6, 9, 28] P-O bond is the dominant components in all P 2p peaks of NPCs. Small fraction of P-C bond also presents, which is believed to also possess ORR activity in literatures. [28] The concentration of each peaks (in at%) are summarized in **Table 2** and **Figure 3**d. Despite possessing similar or even higher concentrations of pyridinic N, graphitic N and P-C bond, NP-TMP and NP-WB are less active than NP-SP. Interestingly, in the binding energy region for Fe 2p peak (from 706 to 735 eV, **Figure 3**f), we found a small peak at around 711 eV only in NP-SP sample. The peak can be ascribed to Fe $2p_{3/2}$ peak, indicating the existence of Fe species [29] and the concentration is around 0.04 at%. To verify the existence of Fe species on the surface of NP-SP, a carefully analysis using aberration-corrected HAADF-STEM was carried out, and the obtained image is shown in **Figure 5**a. Small white dots with angstrom-scale sizes (some of them are indicated by red cycles) can be found throughout the whole material, revealing well-dispersed single-atom Fe. Thus, the Fe single atoms only existed on NP-SP may be responsible for its better ORR activity.

The electronic and structural information of NP-SP is further extracted from the XANES spectra that reflect intense resonance features, arising from excitations of core-level electrons to their unoccupied states. As shown in **Figure 4**a, the C K-edge XANES spectrum has two main features located at 285.5 eV (peak a) and 291.9 eV (peak c). It can be attributed to the 1s

→π* excitation of the out-of-plane C=C bond and the 1s→σ* excitation of the in-plane C-C bond, respectively. [30] The broad feature centered at 288.5 eV (peak b) is also observed between the π* and σ* excitations, originating from the interlayer states after heteroatom doping. It may be ascribed to C-O/N/P bonds in graphitic carbon matrix. [31] **Figure 4**b shows the N K-edge XANES spectrum with four well-resolved peaks at 398.2 eV (peak a_1), 399.2 eV (peak b), 401.0 eV (peak c) and 406.8 eV (peak d). Peak a, b and c are assigned to the π* excitations of the pyridinic (C-N-C), pyrrolic and graphitic (N-3C) type N species, respectively. Notably, the peak a_1 appears a shoulder peak a_2 at higher energy side, suggesting that the partial Fe atoms are bonded to pyridinic N. [32] The Fe L-edge spectrum of NP-SP is shown in **Figure 4**d, which confirms the observation of XPS data that Fe species exist in NP-SP. Fe L-edge spectrum (L_3 edge in the region of 706 eV to 712 eV and L_2 edge in the region of 718 eV to 726 eV) was aroused by electronic transitions between Fe 2p electrons and unoccupied 3d orbitals, and was further split by the ligand field due to the final state effect. [33, 34] In the L_3 edge region, a major peak at around 709.5 eV (peak a_1) and a shoulder peak at around 708.0 eV (peak a_2) can be observed, which suggests more contribution of high spin Fe^{3+} in NP-SP due to possible incorporation of oxygen, as reported in the literature. [33] More evidence can be obtained from the P L-edge XANES spectrum of NP-SP in **Figure 4**c. A broad feature in the range from 135~140 eV splits four peaks: the two peaks a_1 (136.3 eV) and a_2 (137.2 eV) at low energy side were caused by the excitations of 2p electrons (from the L_3 and L_2 edges) to the first unoccupied 3s-like antibonding state, while the peak a_3 (138.6 eV) with a shoulder (a_4) is attributed to the transitions to 3p levels with respect to the mixed characters from oxygen and Fe, suggesting that Fe is also bonded to P. Peak b arising from 142.3 eV can be assigned to the bond with N/C in carbon matrix. [35] The feature at 145.9 eV (peak c) is due to 2p to 3d transitions in elemental P. These observations prove that the binding between Fe and O, N, and P affected the electronic structure of Fe single atoms.
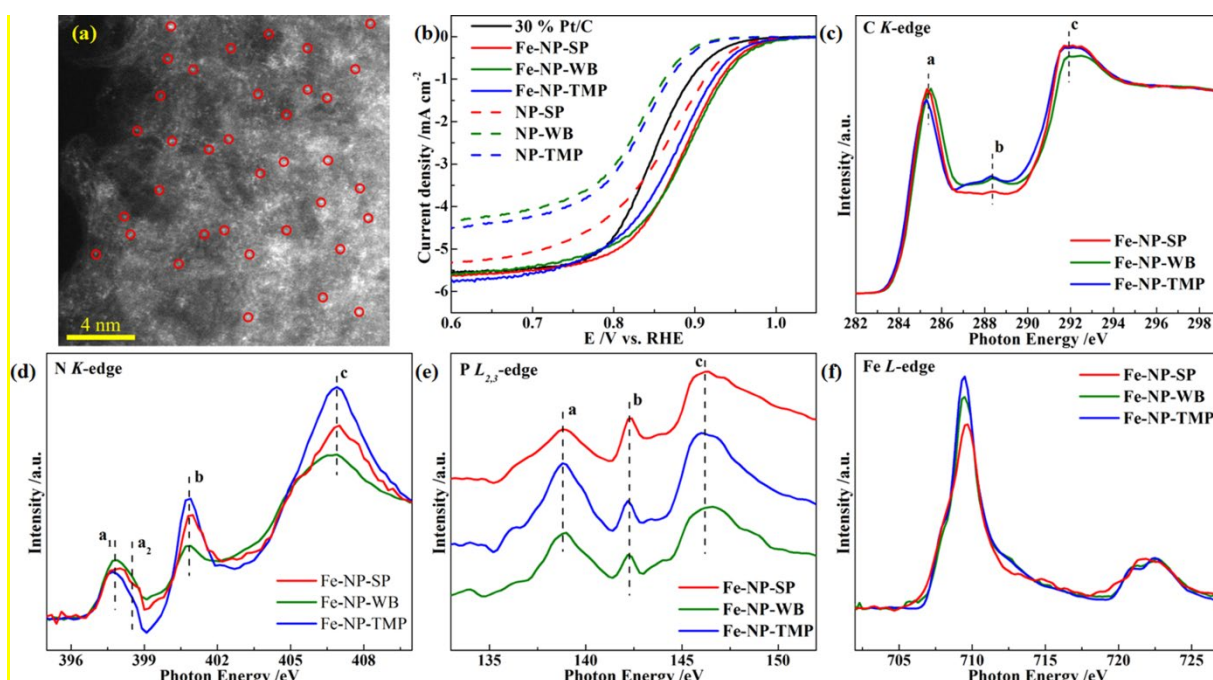
Figure 5. (a) Aberration-corrected HAADF-STEM of NP-SP, in which some of the single atoms are marked by red cycles. (b) LSV curves of Fe-NPCs and NPCs in O_2-saturated 0.1 mol L^{-1} KOH at a scan rate of 10 mV s^{-1} with rotating rate of 1600 r.p.m. in the potential window between 0.6 V to 1.05 V (c) C K-edge, (d) N K-edge, (e) P $L_{2,3}$-edge and (f) Fe L-edge XANES spectra of Fe-NPCs.

Inspired from the results of woody biomass SP, external Fe precursor was introduced into different woody biomass. The electrocatalytic activity of the resultant Fe-NPC catalysts is summarized in **Figure 5**b. Surprisingly, the LSV curves of all Fe-NPC catalysts almost overlapped that E_{onset} of 1.050 V and E_{half} of 0.874 V were achieved, regardless of biomass sources. More importantly, the activities of all Fe-NPCs are greatly improved compare to NPCs, which also outperform the 30 wt% Pt commercial catalyst, suggesting that we successfully update our electrocatalysts by mimicking the natural materials. The XANES of Fe-NPCs was further carried out and the results are shown in **Figure 5**c-f for C K-edge, N K-edge, P $L_{2,3}$-edge and Fe L-edge spectra, respectively. All feature peaks in these spectra are similar to those of NP-SP (**Figure 4**), indicating similar active site structures. All spectra obtained from

different biomass derived catalysts have a high similarity. These results suggested that the effect of different biomass is eliminated after external Fe were introduced. Moreover, the almost identical active sites and almost identical activities achieved may owing to the possible saturation of Fe on the materials. It is worth noting that in N K-edge spectra of Fe-NPCs (**Figure 5**d), the existence of both a_1 and a_2 features again confirmed the bonding between Fe atoms and pyridinic N. [32] It clearly reveals the ability of Fe containing active site for boosting ORR activity. The results open a new avenue to boost ORR activity by synthesis of ORR catalysts from various biomasses through proper doping of N, P and Fe.

To verify the synergetic effect of different dopants, we synthesized catalysts with different dopants derived from WB. The reason for using WB instead of SP as the precursor is to exclude the effect of trace amount of Fe in the biomass. The electrochemical performances are summarized in **Figure S4**a. The activity follows an order of Fe-NP-WB > NP-WB > N-WB > CWB. XANES analysis of the resulted catalysts is shown in **Figure S4**b-d. A strong feature b_2 in the spectrum of CWB indicates that it is an oxygen group abundant material. While with the introduction of reductive atmosphere (and introduction of Fe for Fe-NP-WB) during preparation, the intensity of b_2 decreased and the intensity of feature a (ascribed to the $1s \rightarrow \pi^*$ excitation of the out-of-plane C=C bond) increased. Moreover, the weak b_1 peak can be ascribed to C-N bond. [30] In N *K*-edge spectra (**Figure S4**c), peak a and peak b of Fe-NP-WB shifted towards higher energy, which could be attributed to the electron attracting effect of the existed Fe species. [32] **Figure S4**d shows the XANES P $L_{2,3}$-edge spectra of NP-WB and Fe-NP-WB. The feature a that only existed in the spectrum of Fe-NP-WB can be ascribed to the transitions to 3p orbitals due to the mixed characters from oxygen or metals and forms the Fe-O-P bond when Fe was introduced. [36] These results confirmed the binding between Fe and O/N/P on carbon matrix, and their synergy effects is the origin of the great ORR activity.

The selectivity was studied by measuring the electron transfer numbers through the LSV curves of NPCs at different rotating speeds, as shown in **Figure S5**. The related K-L plots are shown in **Figure S6**. All K-L plots exhibit linear relationships between J^{-1} and $\omega^{-1/2}$, and the average n calculated from these curves are shown in the figure. In terms of electron transfer number n, 30 % Pt/C is still the best, with a very close to four electron transfer value. Among NPCs, NP-TMP possesses the highest n of 3.86 and NP-SP comes in second with n of 3.73, both of which are close to it of 30 % Pt/C, suggesting a comparable efficiency. The results suggest that all the NP catalysts take the efficient 4e$^-$ pathway.
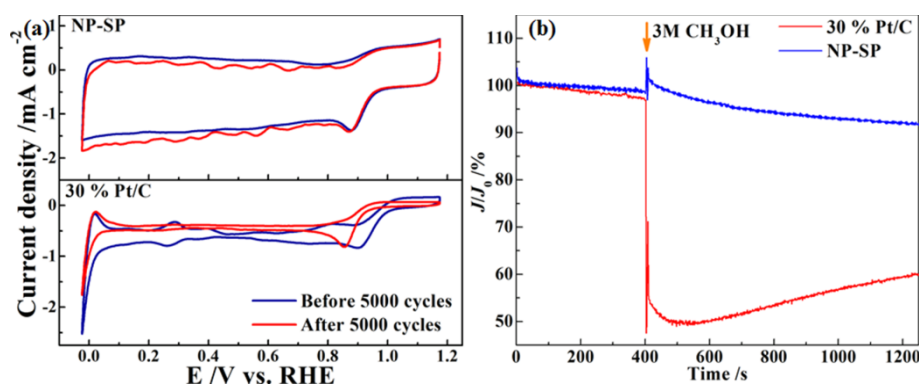

Figure 6. (a) Cyclic voltammograms of NP-SP and 30 % Pt/C before and after the durability test (5000 cycles) in oxygen saturated 0.1 mol L^{-1} KOH aqueous solution at a scan rate of 10 mV s^{-1}. (b) Current-time curves of NP-SP and 30 % Pt/C in oxygen saturated 0.1 mol L^{-1} KOH aqueous solution at 0.7 V while 3 mol L^{-1} CH$_3$OH was added at 400 s.

As the best ORR catalyst among all NPCs, the stability and methanol tolerance of NP-SP were investigated. CVs of NP-SP and 30 % Pt/C with a scan rate of 0.1 V s^{-1} were carried out for 5000 cycles, and the CV curves of them before and after cycling are shown in **Figure 6**a. Obvious shape and reduction peak position changes can be observed from the curves of Pt/C, where the peak position shifted 45 mV towards negative after cycling, indicating a poor long-term stability. For NP-SP, small changes occurred on the CV curve after cycling, with a negligible 7 mV negative shift for the reduction peak, which indicates an excellent stability of

NP-SP catalyst for catalyzing long-term oxygen reduction. When 3 mol L^{-1} CH$_3$OH was introduced after 400 s (indicated by the arrow), the current-time curves at 0.7 V of NP-SP and Pt/C were recorded as shown in **Figure 6**b. Suffering from the crossover effect, the reduction current of Pt/C dropped dramatically after methanol injection, only about 50 % of its initial current remained, similar to those observations in literatures. [13, 37] While the stability of NP-SP is much better where the addition of methanol only affected the current density slightly. The results suggest that cost-effective and sustainable NP-SP electrocatalyst possesses good activity and selectivity as well as excellent methanol cross over resistance, making it an ideal candidate to replace Pt-based catalysts.

3. Conclusion

In summary, we have reported a new class of cost-effective and sustainable Fe-N-P-C electrochemical ORR catalysts directly produced from woody biomass by a simple and scalable impregnation-pyrolysis method in the presence of NH$_3$ and P precursor. The observed significantly better activity of NP-SP is ascribed to trace iron in the sawdust of pine, resulted from atomically dispersed single-atom Fe in the NPC matrix revealed by different characterization techniques such as aberration-corrected HAADF-STEM, XPS and XANES. We demonstrated that the catalytic activity depends significantly on the structure of active sites, and the activity follows an order of Fe-NPC> NPC > NC > C. The highly dispersed single-atom Fe coordinated with N, P and O in carbon matrix possesses the highest ORR activity. All the Fe-NPC catalysts with the introduced external Fe, mimicking the natural materials, possess similar ORR activity regardless of the type of the biomass, which outperformed commercial Pt catalysts. In addition, NP-SP exhibited excellent performances in long-term cycling and methanol tolerance tests. We believe that we have opened a promising new avenue to develop cost effective sustainable ORR catalysts from biomass to replace Pt-based catalysts in alkaline medium for large-scale applications, such as fuel cells and metal-air batteries.

4. Experimental Section

Synthesis of NPC: NPC were produced by an impregnation-pyrolysis method. The biomasses used in the synthesis are sawdust of pine (SP), wood briquette (WB, mixture of wood flakes), and thermo-mechanical pulping biomass fiber (TMP). The properties of these biomass materials are presented in the supporting information. Firstly, biomass (SP, WB or TMP, 6 g) powder was dispersed in H_3PO_4 (sigma-aldrich, 200 mL, 1.5 mol L^{-1}) solution and stirred vigorously for 30 minutes, and then the excess solution was filtered out and the obtained filter cake was dry at room temperature overnight. The dried biomass powder was then transferred into a fix-bed reactor, heated to 1000 °C with a heating rate of 5 °C min^{-1} and kept for 2 hours under a NH_3 flow (50 mL min^{-1}). Note that the temperature is chosen based on Dai's report [6], the effect of pyrolysis temperature will be investigated in the future. After cooling to room temperature, the obtained black powder was reflux in distilled water at 110 °C overnight to remove any residue. After wash and dry with distilled water and ethanol to remove any possible residues, the catalyst powder was obtained. The yield of catalyst produced with this method is around 5 to 10 % based on the woody biomass precursors. Catalysts produced from SP, WB and TMP are denoted as NP-SP, NP-WB and NP-TMP, respectively. To compare with, NCs were produced with the same procedure but using distilled water instead of phosphoric acid during impregnation. The resulted catalysts are denoted as N-SP, N-WB and N-TMP, respectively. CBs were also produced simply by pyrolyzing the biomass powder at 1000 °C under argon flow. The resulted catalysts are denoted as CSP, CWB and CTMP, respectively.

Synthesis of Fe-NPC: Fe-NPCs derived from SP, WB and TMP with intentionally added Fe were also produced with the impregnation-pyrolysis method. A precursor solution containing H_3PO_4 (1.5 mol L^{-1}) and $FeCl_3$ (0.025 mol L^{-1}) was used during the impregnation. The resulted catalysts are denoted as Fe-NP-SP, Fe-NP-WB and Fe-NP-TMP, respectively.

Materials characterization: Field-emission scanning electron microscopy (FE-SEM, Q-200, Hillsboro, USA) was used to investigate the surface morphologies of catalysts. Transmission electron microscopy (TEM) characterizations were conducted using a JEM-2100F (JEOL Ltd, Japan) with an accelerating voltage of 200 kV. The aberration-corrected high-angle annular dark field scanning transmission electron microscopy (HAADF-STEM) images were taken using aberration-corrected FEI Titan Cubed Themis G2 300 with an accelerating voltage of 200 kV. The N_2 sorption isotherms were performed on a Tristar II 3020 (Micromeritics Instruments, USA). Pore size distribution (PDS) was obtained from the isotherm results based on DFT calculation. A degassing step was applied to the catalysts at 200 °C for 12 h under turbomolecular vacuum pumping before the adsorption/desorption measurements. X-ray photoelectron spectrometry (XPS) was performed using a Kratos XSAM 800 spectrometer (Manchester, UK) equipped with an Al Kα X-ray (1486.6 eV, excitation source working at 15 kV). The C 1s peak at 284.6 eV was taken as an internal standard to correct the shift in the binding energy caused by sample charging. X-ray absorption near edge structure (XANES) spectroscopy of C *K*-edge, N *K*-edge, P $L_{2,\,3}$-edge and Fe *L*-edge were performed at the MCD endstation at the beamline BL12B-a in the National Synchrotron Radiation Laboratory (NSRL), Hefei, China. The storage ring of the NSRL was operated at 0.8 GeV with a maximum current of 300 mA. The spectra were recorded at room temperature with an energy step of 0.2 eV and the total electron yield (TEY) detection mode.

Electrochemical tests: The electrochemical oxygen reduction properties of as-obtained catalysts were evaluated with a three-electrode system at ambient condition using a Princeton VersaSTAT potentiostat analyzer (Princeton Applied Research). The working electrode was prepared by coating a catalyst film onto a glassy carbon rotating-disk electrode (RDE, with a diameter of 5 mm). The catalyst ink used in the coating was produced by dispersing catalyst (4 mg) in ethanol solution (2 mL) containing Nafion (5 wt%, 16 μL, Alfa Aesar, D520 dispersion) and sonicated for 120 min. The as-obtained catalyst ink (50 μL) was coated onto the glassy

carbon disk drop by drop, and the as-obtained electrode (with catalyst loading of 0.5 mg cm^{-2}) was dried at room temperature overnight. The counter and reference electrodes are Pt wire and Ag/AgCl electrode (3.5 mol L^{-1} KCl) respectively. KOH aqueous solution (0.1 mol L^{-1}) was used as electrolyte. Argon or oxygen was bubbling into the electrolyte 30 min prior the electrochemical tests according to the demands. To compare with, a Pt/C (30 wt% Pt on Vulcan carbon black, Fuel Cell Store) coated glassy carbon electrode was also prepared according to the same procedure described above, the catalyst ink (10 µL) was coated onto the electrode. All measured potentials were converted to potential vs. reversible hydrogen electrode (RHE) according to the following equation, unless specified: [6, 38]

$$E_{vs\ RHE} = E_{vs\ Ag/AgCl} + E_{ø\ Ag/AgCl} + 0.059\ pH \tag{1}$$

Where $E_{vs\ RHE}$ is the potential vs. RHE, $E_{vs\ Ag/AgCl}$ is the potential vs. Ag/AgCl and $E_{ø\ Ag/AgCl}$ is the potential of Ag/AgCl electrode respect to the standard hydrogen electrode. The Koutechy-Levich (K-L) equation was used to calculate the electron transfer number (n) per oxygen molecule in ORR process at the electrode: [6, 39]

$$B = 0.2nFC_0D_0^{2/3}v^{-1/6} \tag{2}$$

$$1/J = 1/J_L + 1/J_K = 1/(B\omega^{1/2}) + 1/J_K \tag{3}$$

Where J is the measured current density, J_L is the diffusion limiting current density, J_K is the kinetic limiting current density, ω is the rotating speed in rpm, F is the Faraday constant (96485 C mol^{-1}), D_0 is the diffusion coefficient of oxygen in 0.1 mol L^{-1} KOH (1.9×10^{-5} cm^2 s^{-1}), v is the kinetic viscosity (0.01 cm^2 s^{-1}), and C_0 is the buck concentration of oxygen (1.2×10^{-3} mol L^{-1}).

Supporting Information

Supporting Information is available from the Wiley Online Library or from the author.

Conflicts of interest

There are no conflicts to declare.

Acknowledgements

Received: ((will be filled in by the editorial staff))
Revised: ((will be filled in by the editorial staff))
Published online: ((will be filled in by the editorial staff))

References

[1]   Y. Yan, B. Y. Xia, B. Zhao, X. Wang, *J. Mater. Chem. A* **2016**, *4*, 17587.

[2]   a) M. Chiwata, H. Yano, S. Ogawa, M. Watanabe, A. Iiyama, H. Uchida, *Electrochemistry* **2016**, *84*, 133; b) D. Raciti, J. Kubal, C. Ma, M. Barclay, M. Gonzalez, M. Chi, J. Greeley, K. L. More, C. Wang, *Nano Energy* **2016**, *20*, 202; c) V. Beermann, M. Gocyla, E. Willinger, S. Rudi, M. Heggen, R. E. Dunin-Borkowski, M.-G. Willinger, P. Strasser, *Nano letters* **2016**, *16*, 1719.

[3]   J. Zhang, L. Qu, G. Shi, J. Liu, J. Chen, L. Dai, *Angew. Chem., Int. Ed.* **2016**, *55*, 2230.

[4]   X. Bai, E. Zhao, K. Li, Y. Wang, M. Jiao, F. He, X. Sun, H. Sun, Z. Wu, *Carbon* **2016**, *105*, 214.

[5]   a) S. Chao, M. Geng, *Int. J. Hydrogen Energy* **2016**, *41*, 12995; b) X. Fu, J. Y. Choi, P. Zamani, G. Jiang, M. A. Hoque, F. M. Hassan, Z. Chen, *ACS Appl. Mater. Interfaces* **2016**, *8*, 6488; c) F. Charreteur, F. Jaouen, S. Ruggeri, J.-P. Dodelet, *Electrochim. Acta* **2008**, *53*, 2925.

[6]   J. Zhang, Z. Zhao, Z. Xia, L. Dai, *Nat. Nanotechnol.* **2015**, *10*, 444.

[7]   W. Yuan, W. Xu, A. Xie, H. Zhang, C. Wang, Y. Shen, *Energy* **2017**, *141*, 1324.

[8]   a) Y. Lu, L. Wang, K. Preuß, M. Qiao, M.-M. Titirici, J. Varcoe, Q. Cai, *J. Power Sources* **2017**, *372*, 82; b) K. Preuss, L. Tănase, C. Teodorescu, I. Abrahams, M.-M. Titirici, *J. Mater. Chem. A* **2017**, *5*, 16336.

[9]   G.-L. Chai, K. Qiu, M. Qiao, M.-M. Titirici, C. Shang, Z. Guo, *Energy Environ. Sci.* **2017**, *10*, 1186.

[10]   a) J. Masa, A. Zhao, W. Xia, Z. Sun, B. Mei, M. Muhler, W. Schuhmann, *Electrochem. Commun.* **2013**, *34*, 113; b) J. Masa, W. Xia, M. Muhler, W. Schuhmann, *Angew. Chem., Int. Ed.* **2015**, *54*, 10102; c) J. Xu, M. Wang, N. P. Wickramaratne, M. Jaroniec, S. Dou, L. Dai, *Adv. Mater.* **2015**, *27*, 2042.

[11]   X. Cui, S. Yang, X. Yan, J. Leng, S. Shuang, P. M. Ajayan, Z. Zhang, *Adv. Funct. Mater.* **2016**, *26*, 5708.

[12]   a) J. Yang, D.-J. Liu, N. N. Kariuki, L. X. Chen, *Chem. Commun.* **2008**, *3*, 329; b) W. Liu, L. Zhang, X. Liu, X. Liu, X. Yang, S. Miao, W. Wang, A. Wang, T. Zhang, *J. Am. Chem. Soc.* **2017**, *139*, 10790.

[13]   C. Zhu, S. Fu, J. Song, Q. Shi, D. Su, M. H. Engelhard, X. Li, D. Xiao, D. Li, L. Estevez, D. Du, Y. Lin, *Small* **2017**, *13*, 1603407.

[14]   I. S. Amiinu, J. Zhang, Z. Kou, X. Liu, O. K. Asare, H. Zhou, K. Cheng, H. Zhang, L. Mai, M. Pan, S. Mu, *ACS Appl. Mater. Interfaces* **2016**, *8*, 29408.

[15]   a) H. Yu, L. Shang, T. Bian, R. Shi, G. I. Waterhouse, Y. Zhao, C. Zhou, L. Z. Wu, C. H. Tung, T. Zhang, *Adv. Mater.* **2016**, *28*, 9454; b) P. Yin, T. Yao, Y. Wu, L. Zheng, Y. Lin, W. Liu, H. Ju, J. Zhu, X. Hong, Z. Deng, G. Zhou, S. Wei, Y. Li, *Angew. Chem., Int. Ed.* **2016**, *55*, 10800.

[16]   a) X. Li, Y. Fang, X. Lin, M. Tian, X. An, Y. Fu, R. Li, J. Jin, J. Ma, *J. Mater. Chem. A* **2015**, *3*, 17392; b) X. Wang, J. Zhou, H. Fu, W. Li, X. Fan, G. Xin, J. Zheng, X. Li, *J. Mater. Chem. A* **2014**, *2*, 14064; c) W. Chaikittisilp, K. Ariga, Y. Yamauchi, *J. Mater. Chem. A* **2013**, *1*, 14.

[17]   R. Li, Z. Wei, X. Gou, *ACS Catal.* **2015**, *5*, 4133.

[18]   L. Tao, Q. Wang, S. Dou, Z. Ma, J. Huo, S. Wang, L. Dai, *Chem. Commun.* **2016**, *52*, 2764.

[19]   S. Chu, Y. Cui, N. Liu, *Nat. Mater.* **2017**, *16*, 16.

[20]   S. K. Ritter, *Chem. Eng. News* **2017**, *95*, 26.

[21]   a) H.-W. Liang, X. Zhuang, S. Brüller, X. Feng, K. Müllen, *Nat. Commun.* **2014**, *5*, 4973; b) J. Liang, X. Du, C. Gibson, X. W. Du, S. Z. Qiao, *Adv. Mater.* **2013**, *25*, 6226.

[22]   a) M. Shao, Q. Chang, J. P. Dodelet, R. Chenitz, *Chem. Rev.* **2016**, *116*, 3594; b) C. Zhu, H. Li, S. Fu, D. Du, Y. Lin, *Chem. Soc. Rev.* **2016**, *45*, 517.

[23]   a) S. Ratso, I. Kruusenberg, U. Joost, R. Saar, K. Tammeveski, *Int. J. Hydrogen Energy* **2016**, *41*, 22510; b) I. M. Rocha, O. S. G. Soares, D. M. Fernandes, C. Freire, J. L. Figueiredo, M. F. R. Pereira, *ChemistrySelect* **2016**, *1*, 2522; c) H. Yu, L. Shang, T. Bian, R. Shi, G. I. Waterhouse, Y. Zhao, C. Zhou, L. Z. Wu, C. H. Tung, T. Zhang, *Adv. Mater.* **2016**, *28*, 5080.

[24]   K. Gong, F. Du, Z. Xia, M. Durstock, L. Dai, *science* **2009**, *323*, 760.

[25]   a) Y. Liang, Y. Li, H. Wang, J. Zhou, J. Wang, T. Regier, H. Dai, *Nat. Mater.* **2011**, *10*, 780; b) H. Xue, J. Tang, H. Gong, H. Guo, X. Fan, T. Wang, J. He, Y. Yamauchi, *ACS Appl. Mater. Interfaces* **2016**, *8,* 20766.

[26]   a) Z. L. Wu, P. Zhang, M. X. Gao, C. F. Liu, W. Wang, F. Leng, C. Z. Huang, *J. Mater. Chem. B* **2013**, *1*, 2868; b)X. Teng, C. Ma, C. Ge, M. Yan, J. Yang, Y. Zhang, P. C. Morais, H. Bi, *J. Mater. Chem. B* **2014**, *2*, 4631; c) J. Wu, C. Jin, Z. Yang, J. Tian, R. Yang, *Carbon* **2015**, *82*, 562.

[27]   H. Jiang, Y. Zhu, Q. Feng, Y. Su, X. Yang, C. Li, *Chem-Eur J.* **2014**, *20*, 3106.

[28]   M. Li, T. Liu, X. Bo, M. Zhou, L. Guo, S. Guo, *Nano Energy* **2017**, *33*, 221.

[29]   C. Domínguez, F. Perez-Alonso, M. A. Salam, S. A. Al-Thabaiti, M. A. Peña, L. Barrio, S. Rojas, *J. Mater. Chem. A* **2015**, *3*, 24487.

[30] C.-H. Chuang, Y.-F. Wang, Y.-C. Shao, Y.-C. Yeh, D.-Y. Wang, C.-W. Chen, J. Chiou, S. C. Ray, W. Pong, L. Zhang, *Sci. Rep.* **2014**, *4*, 4525.

[31] H. B. Yang, J. Miao, S.-F. Hung, J. Chen, H. B. Tao, X. Wang, L. Zhang, R. Chen, J. Gao, H. M. Chen, *Sci. Adv.* **2016**, *2*, e1501122.

[32] P. Chen, T. Zhou, L. Xing, K. Xu, Y. Tong, H. Xie, L. Zhang, W. Yan, W. Chu, C. Wu, *Angew. Chem., Int. Ed.* **2017**, *56,* 610.

[33] J. Zhou, P. N. Duchesne, Y. Hu, J. Wang, P. Zhang, Y. Li, T. Regier, H. Dai, *Phys. Chem. Chem. Phys.* **2014**, *16*, 15787.

[34] D. Liu, C. Wu, S. Chen, S. Ding, Y. Xie, C. Wang, T. Wang, Y. A. Haleem, Z. ur Rehman, Y. Sang, Q. Liu, X. Zheng, Y. Wang, B. Ge, H. Xu, L. Song, *Nano Res.* **2018**, *11*, 2217.

[35] Y. Lin, L. Yang, Y. Zhang, H. Jiang, Z. Xiao, C. Wu, G. Zhang, J. Jiang, L. Song, *Adv. Energy Mater.* **2018**, 1703623.

[36] a) J. Kruse, P. Leinweber, K.-U. Eckhardt, F. Godlinski, Y. Hu, L. Zuin, *J. Synchrotron Radiat.* **2009**, *16*, 247; b) S. Yang, D. Wang, G. Liang, Y. M. Yiu, J. Wang, L. Liu, X. Sun, T.-K. Sham, *Energy & Environ. Sci.* **2012**, *5*, 7007.

[37] M. Kim, H. S. Kim, S. J. Yoo, W. C. Yoo, Y.-E. Sung, *J. Mater. Chem. A* **2017**, *5*, 4199.

[38] M. Ma, S. You, W. Wang, G. Liu, D. Qi, X. Chen, J. Qu, N. Ren, *ACS Appl. Mater. Interfaces* **2016**, *8*, 32307.

[39] F. Lou, M. E. M. Buan, N. Muthuswamy, J. C. Walmsley, M. Rønning, D. Chen, *J. Mater. Chem. A* **2016**, *4*, 1233.

Nitrogen and phosphorus decorated sustainable carbocatatlysts with excellent ORR activities that outperformed many state-of-the-art electrocatalysts are produced only from woody biomass using a simple impregnation-pyrolysis method. Aberration-corrected HAADF-STEM revealed that the atomically dispersed Fe-N-P-C complex structure formed with trace Fe species initially existed in woody biomass is responsible for the high activity.

Keyword: sustainable carbocatalyst, nitrogen- and phosphorus-modified biomass, atomically dispersed iron electrocatalyst, oxygen reduction

Yahao Li[#], Daobin Li[b#], Jie Gan, Xuezhi Duan[*], Ketao Zang, Magnus Rønning, Li Song, Jun Luo, De Chen[*]

Sustainable and atomically dispersed iron electrocatalysts derived from nitrogen- and phosphorus-modified woody biomass for efficient oxygen reduction